IOSR Journal Of Applied Geology And Geophysics (IOSR-JAGG)
E-ISSN: 2321–0990, P-ISSN: 2321–0982.Volume 12, Issue 4 Ser. I (July. – August. 2024), 30-46
Www.Iosrjournals.Org

Remote Sensing And Spectral Characterization Of Clay Minerals In Mui Basin, Kenya

Benard K. Limo[1*], Patrick C. Kariuki[2], Douglas O. Onyancha[3], Eliud M. Mathu[4], Lincoln K. Githenya[5], Duncan L. Ambembo[6]

Institute Of Geothermal Training And Research, Dedan Kimathi University Of Technology, Nyeri, Kenya
Institute Of Geothermal Training And Research, Dedan Kimathi University Of Technology, Nyeri, Kenya
Department Of Chemistry, Dedan Kimathi University Of Technology, Nyeri, Kenya
Department Of Geology And Meteorology, South Eastern Kenya University, Kitui, Kenya
Institute For Applied Geosciences, Kit-Karlsruhe Institute Of Technology, Karlsruhe, Germany
State Department For Energy, Ministry Of Energy And Petroleum, Nairobi, Kenya

Abstract
Clay minerals possess distinctive physiochemical attributes, notably their water absorption capacities and propensity to signify soil swelling behavior. Identifying and quantifying these components are essential for engineering endeavors. Infrared spectroscopy, specifically in the short-wave infrared (SWIR) domain, has proven to be a productive and widespread instrument for analyzing clay minerals due to its diagnostically informative SWIR spectral details. Water molecules (H_2O) and hydroxyl groups (OH) generate diagnostic absorptions in clay minerals within the SWIR wavelength region. This study focuses on the petrological, mineralogical, spectral, and economic characteristics of clay deposits in the Mui Basin in Kenya. By employing Landsat 8 OLI and TIRS satellite images and Near-Infrared (NIR) spectral analysis, we aim to comprehend the feasibility of utilizing these resources industrially. Advanced image enhancement techniques, including band combinations, band ratios, Principal Component Analysis (PCA), and image classification, were implemented to maximize the extracted information content from the datasets. Soil samples were subsequently examined using NIR spectra obtained via the Multi-Purpose Analyzer (MPA) manufactured by Bruker Germany at CIFOR-ICRAF's Soil-Plant Spectral Diagnostic Laboratory in Nairobi. Band ratio enhancement strategies were deployed to detect hydrothermal alteration zones and distinguish among clay minerals. Two primary clay types—smectite and halloysite were discovered within the Mui Basin. Smectite clays, characterized by specific spectral signatures at 1.415µm, 1.911µm, and 2.209µm, were present in several borehole locations throughout the basin. Smectite clays find applications in sectors ranging from oil and geothermal drilling to agricultural and construction industries. By comprehensively examining the Mui Basin's clay deposits, our findings contributed valuable insights into the characterization, utilization, and management of these natural resources in Kenya and beyond.

Keywords: *Spectroscopy, remote sensing, short wave infrared (SWIR), clays*

Date of Submission: 15-08-2024 Date of Acceptance: 25-08-2024

I. Introduction

Remote sensing and spectroscopy have become highly influential, widely used tools for investigating mineral deposits, mainly when minerals act as indicators or pathfinders[1];[2]; [3]. Spectroscopy's potential lies in the diagnostic spectral data within the 0.7–3 µm Near Infrared (NIR) to short-wave infrared (SWIR) region, extensively applied in mineral exploration[4]. Studies have shown this information can identify minerals' presence, composition, and associated properties.

Clay minerals possess distinct physicochemical properties that facilitate their differentiation. Particularly in construction, the focus has been on smectite, illite, and kaolinite characteristics due to their water absorption tendencies and their role as indicators of soil swelling properties, which are critical for engineering projects. [5]. Clay minerals have diverse industrial applications. They are used in foundry sand and desiccants to absorb moisture [6]. In agriculture, clay is added to drought-prone soils to retain moisture [7]. It also acts as an absorbent for toxic heavy metals in water treatment[8]. In construction, clay is used in earthen dams and levees to prevent fluid leakage [9]. Bentonite and smectite clays, particularly in geothermal drilling, play a crucial role. Bentonite is a critical component in water-based drilling muds, providing viscosity and aiding in the removal of drill cuttings [10]; [11]. Smectite clays, like montmorillonite in bentonite, help form a thin, low-permeability filter cake to prevent fluid loss[11].

The primary aim of this research endeavor is to investigate the various clay types present in the Mui Basin and assess their potential for use in geothermal drilling and a range of industrial applications. To achieve this objective, the study employs remote sensing and spectral analysis techniques to study clays' petrology, geochemistry, and physical properties. Obtaining a comprehensive understanding of these characteristics is crucial for determining the feasibility of these resources for industrial utilization, particularly in enhancing geothermal energy production.

Location

The study area is in the southeastern part of Kenya, specifically in Kitui County (figure 1). It is located within UTM zone 37 South and is delimited by the geographical coordinates of longitudes 38° 9' 30" E to 38° 15' 5" E and latitudes 0° 51' 57" S to 1° 28' 22" S in the Southern Hemisphere. The area spans approximately 817 square kilometers. Access to the region can be gained via the Nairobi-Thika-Mwingi road or the Nairobi-Machakos-Kitui-Zombe road, and the distance from Nairobi City to the study area is roughly 200 kilometers. From Mombasa town, the area can be accessed via Mombasa- Kibwezi-Kitui-Mwingi Road, which is approximately 510 kilometers.

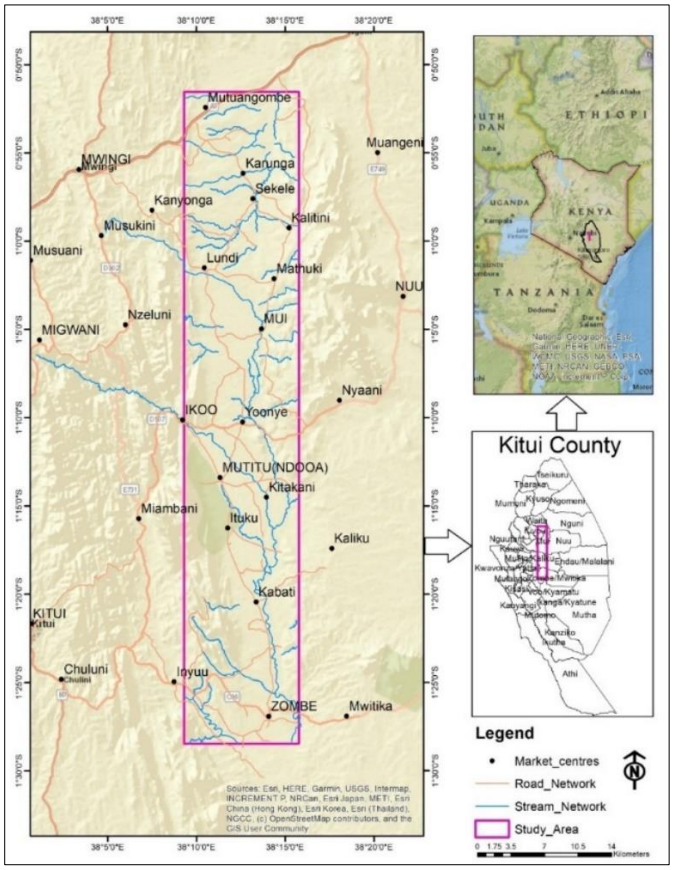

Figure 1: Approximate location of the study area

Geological Setting of Mui Basin Area

The Mui basin is predominantly underlain by high-grade metamorphic rocks of the Precambrian period[12]. The assemblage primarily comprises migmatites, granulites, schists, and both meta-intrusive and meta-extrusive rocks[13]. Geologically, these formations are commonly recognized as the Mozambique belt rocks, displaying a distinct NNW-SSE strike orientation[12]. The Basin exhibits significant variation as one moves from west to east.

Within the confines of the basin itself, the geological landscape is predominantly shaped by quaternary sediments, which blanket the underlying basement rocks. These sediments encompass a diverse range of materials, including carbonaceous marcasite clays, shales, sandstones, various types of sands, lignite coal, and superficial soils[14];[15]. Notably, these sedimentary layers are believed to have been deposited in a lacustrine environment, as elucidated by Mathu in 1992 (p. 63). Figure 2 illustrates Mui Basins's geology based on studies by Crowther (1957), Sanders (1954), and Mathu (1992).

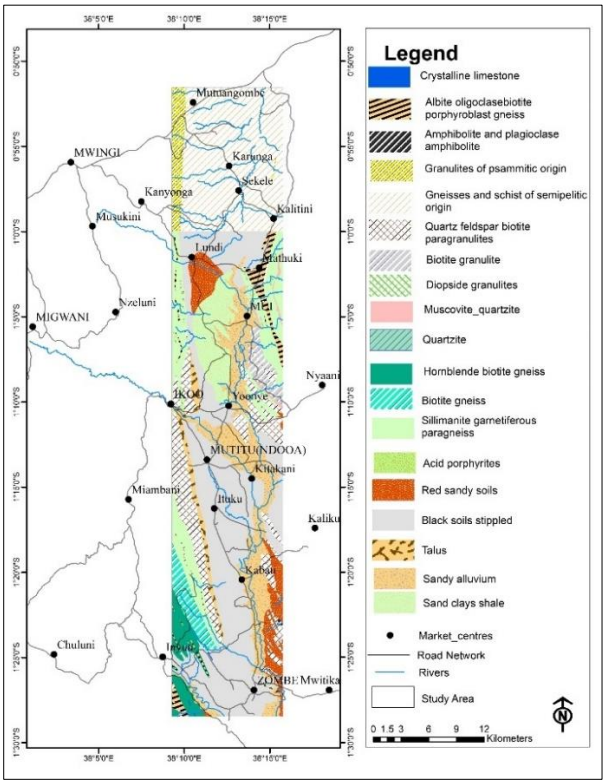

Figure 2: Geological map of the Mui Basin area

II. Materials And Methods

The mapping and identification of clay minerals in the Mui Basin area necessitated a comprehensive exploration of the entire basin. During this process, physical observations of the lithologies encountered were documented, and soil and rock samples were collected. These samples were subsequently analyzed using a reflectance spectroscopy instrument at the Soil-Plant Spectral Diagnostic Laboratory within the premises of CIFOR-ICRAF in Nairobi. Furthermore, the study involved the processing and interpreting Landsat 8 OLI satellite imagery.

Fieldwork/soil sampling

Fieldwork in the Mui Basin area was carried out in July and October 2022. Seventy-seven samples were gathered from the region, comprising 64 rock samples from the eight Boreholes drilled by the Ministry of Energy and 13 soil samples obtained from excavated pits in the area. These samples are representative of the entire study area. The location of each sample was carefully documented in a field notebook, together with the corresponding geographical coordinates and field photographs. The Boreholes were logged, and the various lithologies encountered in the Boreholes were recorded and organized in an Excel datasheet.

Processing and interpretation of Landsat 8 OLI TIRS satellite imagery

The Landsat 8 OLI and TIRS satellite image acquired on August 26, 2021, was obtained from the United States Geological Survey (USGS) website (https://lpdaac.usgs.gov). This image was chosen because it was taken during the season when the green vegetation cover was at its lowest and the cloud cover was minimal, amounting to less than 20%. A Landsat-8/OLI image with a terrain-corrected level 1T and a spatial resolution of approximately 30 meters was obtained from the USGS website. The data had already been subjected to atmospheric correction by the data provider, so no additional correction was performed. The data provider, the USGS website, had converted the image to the appropriate WGS 84 datum, UTM zone 37 South, and projection units in meters. The data was only subsetted using a shapefile of the study area for clipping purposes. The following sections will discuss this study's image processing techniques and analysis. The methodology was carried out utilizing ESRI's ArcGIS 10.8 and ArcGIS Pro software packages.

Colour composite

Color composite imaging is a process in which various spectral bands are combined into a single image using the red, green, and blue channels. This technique is employed to enhance the visibility of specific features based on their spectral reflectance properties, such as rocks and alteration minerals [16]. By assigning different

bands to the red, green, and blue components, this approach enables the visual representation of multispectral data in a way that highlights distinct features. A false-color composite (FCC) is an image created by combining visible bands with other bands, such as infrared bands, or by combining only the infrared bands, thus enhancing the spectral characteristics of the bands. On the other hand, a true color composite is formed by combining three visible bands of the spectrum corresponding to red, green, and blue. In color composite imaging, bands are assigned based on the spectral properties of the rocks and alteration minerals to be revealed. This technique enables the visual separation and contrast between different surfaces when displayed as a red, green, and blue image. The resulting image is a false-color composite that preserves morphological features and displays different lithological units in various colors.

Band ratio

Band ratio (BR) is a straightforward technique utilized to enhance the subtle differences in the spectral reflectance of rocks and soils by mitigating the impact of topography [17]. This method involves dividing two bands with the highest reflectance and absorption of the same material (see figure 3), allowing for more precise differentiation between various surface features based on their spectral characteristics [16]. Researchers can highlight specific materials or features in remote sensing data by applying band ratios, aiding in geological analysis and land cover classification.

$$\text{Band Ratio} = \frac{\text{Band with high reflectance feature}}{\text{Band with high absorption feature}}$$

Figure 3: Formular for band ratios

As Sabins (1999) discussed, the band ratio technique involves dividing the digital number (DN) value of one band by the digital number value of another band. This technique helps enhance important features, such as lineaments, that may not be apparent in the raw band. Additionally, band ratios convey the spectral or color characteristics of image features, regardless of variations in scene illumination conditions [18]. Depending on the study's goals, various types of band ratios can be employed for different purposes, such as lithological mapping or alteration discrimination. The choice of bands depends on their spectral reflectance and the positions of the mapped absorption minerals. In this study, for instance, Landsat-8 bands with high spectral reflectance for iron minerals enhanced alteration zones from various intrusions in the area.

Principal component analysis

Principal component analysis (PCA) is an image enhancement technique that displays maximum contrast from several spectral bands using three primary display colors. PCA is a method of identifying patterns in data and expressing them in a way that highlights their similarities and differences [19]. Multispectral image data is typically strongly correlated from one band to the other [20]This led to data redundancy due to the similar visual appearance of different bands. PCA reduces this data redundancy by transforming the original data onto new orthogonal principal component axes, producing an uncorrelated image with higher contrast than the original bands [21]. The number of output principal components (PCs) equals the number of input spectral bands. PC1 highlights features common to all input bands (topography) and often displays crucial structural information. PC2 is orthogonal to PC1 in the n-dimensional space and highlights the spectral differences between visible and infrared spectral bands [21]. PC3 includes the third most variability and is orthogonal to the other two PCs.

Image classification

In remote sensing, image classification involves attributing individual pixel elements or fundamental imagery units to distinct categorical labels. This procedure aims to aggregate homogeneous pixels derived from remotely acquired datasets into coherent classes aligned with users' interests through inter-pixel comparisons against known identity reference samples. The efficacy of supervised classification hinges upon selecting appropriate training sites; a more significant number of such sites typically yields improved outcomes [22].

The study employed a color composite of the Landsat 8 Operational Land Imager (OLI) utilizing Principal Component Analysis (PCA)-derived principal components PC3, PC2, and PC1 for red, green, and blue channels respectively, resulting in a thematic map depicted in Figure 9. Supervised classification techniques were applied to these images, wherein predefined schemas or class categories were established. ArcGIS 10.8's geometry calculator tool calculated the total surface area covered by clays in the study area.

Sample preparation

To begin with, all the samples collected from the field were transferred to a drying room and arranged systematically on drying shelves to guarantee optimal air circulation at a temperature of roughly 40°C. Throughout this procedure, stringent measures were employed to ensure that the sample labels remained affixed to their corresponding samples, thus preventing any confusion or incorrect identifications. After drying, the samples were manually crushed and sieved through a 2mm screen, ensuring a homogenized composition. This sieving process effectively removed stones and other extraneous substances, yielding a uniform sample that could be easily handled in the laboratory.

The following step involved the process of quartering the sample. This was accomplished by vertically inserting a ruler through the center of the sample pile and dividing it into two halves. Each of these halves was then separated into two portions, effectively resulting in the sample being quartered. A subset of the quartered sample, weighing approximately 15g, was milled to a particle size of 0.5mm utilizing a Restch RM 200 machine. The remaining soil sample was saved for potential future reference and additional analysis.

Spectral analysis

All the clay samples collected from the field were analyzed for various chemical properties using near-infrared (NIR) spectra, which were recorded with the Multi-Purpose Analyzer (MPA) module (Bruker Germany) at CIFOR-ICRAF's Soil-Plant Spectral Diagnostic Laboratory at ICRAF in Nairobi (See figure 4).

The NIR spectral analysis technique involved shining near-infrared light on the samples and capturing the diffused and reflected light into a raw file known as the interferogram within the electromagnetic spectrum range of 12,500cm^{-1} to 4,000cm^{-1} wavenumbers range (Hauff, 2008). The recorded spectrum displayed the analyzed samples' qualitative and quantitative chemical aspects.

The Multi-Purpose Analyzer module was explicitly designed for diffuse reflection and transmission measurements. When near-infrared light is incident on a rough or matte surface, two types of reflection occur: specular reflection (where the light reflects directly off the surface) and diffuse reflection (where the IR light penetrates the sample surface and is partly diffusely reflected in all directions due to the rough surface). The optics of the diffuse reflection accessory were optimized to detect diffusely reflected light while minimizing detection of specular reflected light.

The analysis technique employed, known as Diffuse Reflectance Infrared Fourier Transform Spectroscopy (DRIFTS), utilizes the phenomenon of diffuse reflection in FT-IR spectroscopy[23]. One key advantage of this technique is its ability to analyze strongly scattering and absorbing samples, which is not readily achievable with transmission measurements, while also providing high signal intensity. Figure 3 illustrates a sample ready for spectral analysis at the ICRAF spectral laboratory in Nairobi.

Figure 4: Soil samples in a laboratory trolley are ready for analysis at the ICRAF spectral laboratory.

III. Results

Remote Sensing

The six nonthermal bands of Landsat 8 OLI and TIRS satellite acquired on August 26, 2021, underwent comprehensive multivariate image statistical analysis to identify redundancies. Following this, advanced image enhancement techniques were systematically applied to optimize the data's utility, including band combinations, band ratios, principal component analysis (PCA), and image classification. These enhancements collectively

aimed to extract maximum information content from the dataset, ensuring that the resulting imagery, refined through careful processing, provided an enriched basis for insightful analysis and understanding.

Univariate statistics

Table 1: univariate analysis of seven bands of Landsat 8 OLI from the study area

Band Number	Band 1	Band 2	Band 3	Band 4	Band 5	Band 6	Band 7
Min	9018.00	7999.00	6691.00	6063.00	5356.00	4651.00	4843.00
Max	51647.00	53715.00	53825.00	56566.00	59670.00	60925.00	64745.00
Mean	12061.46	11463.99	11257.85	12604.15	16617.83	19165.41	15201.05
Std	4252.11	4456.78	4473.18	4690.71	4725.46	3960.07	3357.94

The results of the univariate statistical analysis presented in Table 1 indicate that Band 1 has the lowest minimum value of 9018.00, while Band 7 has the highest minimum value of 4843.00. Furthermore, Band 7 has the highest maximum value of 64745.00, while Band 1 has the lowest maximum value of 51647.00. These findings illustrate the range and upper limit of values for each band. Additionally, Band 6 has the highest mean value of 19165.41, signifying the average value across the dataset. Conversely, Band 3 has the lowest mean value of 11257.85.

Band 5 displays the most significant standard deviation of 4725.46, indicating the disparity of the data points from the mean. Conversely, Band 7 boasts the lowest standard deviation of 3357.94. The elevated standard deviations in Bands 5 and 6 suggest increased variability in the data, which may be influenced by various surface characteristics or conditions. In contrast, despite its high maximum value, Band 7 exhibits the most consistent reflectance values across different observations, as evidenced by its low standard deviation.

Multivariate statistics

Table 2: Correlation matrix of the seven bands of Landsat 8 OLI from the study area

Layer	Band 1	Band 2	Band 3	Band 4	Band 5	Band 6	Band 7
Band 1	1.00	1.00	0.99	0.97	0.91	0.61	0.57
Band 2	1.00	1.00	0.99	0.97	0.92	0.63	0.59
Band 3	0.99	0.99	1.00	0.99	0.95	0.69	0.65
Band 4	0.97	0.97	0.99	1.00	0.97	0.77	0.74
Band 5	0.91	0.92	0.95	0.97	1.00	0.84	0.79
Band 6	0.61	0.63	0.69	0.77	0.84	1.00	0.98
Band 7	0.57	0.59	0.65	0.74	0.79	0.98	1.00

The results of the multivariate statistical analysis presented in Table 2 indicate that bands 1, 2, 3, 4, and 5 exhibit high levels of correlation with one another (ranging from 0.90 to 1.00), suggesting that they capture similar spectral information. Additionally, bands 6 and 7 exhibit a high level of correlation with each other (0.98), indicating that they capture nearly identical information. The moderate to high correlations between bands 6 and 7 and 1 through 5 (ranging from 0.57 to 0.84) suggest some shared but distinct information among these bands. Among the pairs of bands, the lowest correlation of 59% was observed between bands 2 and 7, followed by the band between 2 and 6 with a correlation of 63%. This makes bands 2 and 7 the most useful in distinguishing differences in spectral information among surface materials within the study area. The high correlations between specific band pairs are attributed to differences in soil reflectance, diverse land cover types, and atmospheric effects [24]; [25].

Colour composite

Several color composites were created to aid in differentiating between bare land, hydrothermally altered rocks, and vegetation. Among these, false-color composite band 5,6,7 RGB (figure 5B) was deemed the most effective combination, as it produced satisfactory results. In false-color image 5,6,7, the color red represents healthy vegetation, the light blue color represents outcrops, bare land, and sands, the dark blue color represents hydrothermally altered rocks, and the light green color represents unhealthy vegetation.

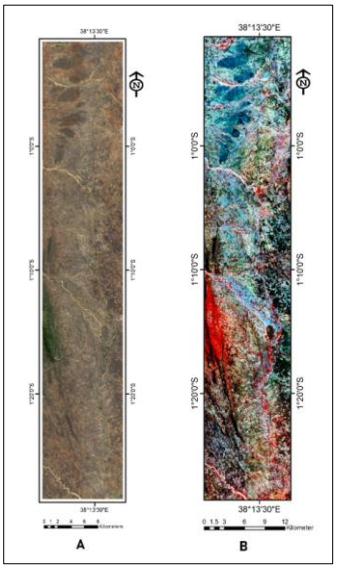

Figure 5: Displays two different compositions. The first composition, A, is a true color composite of bands 4-3-2 in RGB, with green representing vegetation, brown and dark brown representing soils, and light brown representing sand. The second composition, B, is a false-color composite of bands 5-6-7 in RGB, with yellowish green representing clays and hydroxyl minerals, red representing healthy vegetation, and blue representing cultivated or barren land.

Band Rationing

One of the image enhancement techniques that was used to detect hydrothermal alteration zones in the study area is band rationing. Band ratios are very effective for enhancing certain features that cannot be seen in the raw band[26]. The operation is done by dividing the brightness values corresponding to the crests and trough of reflectance curve of one band by that of another band thereby improving the contrast between the features and compositional information while suppressing unwanted information about the study area[3, p. 4].

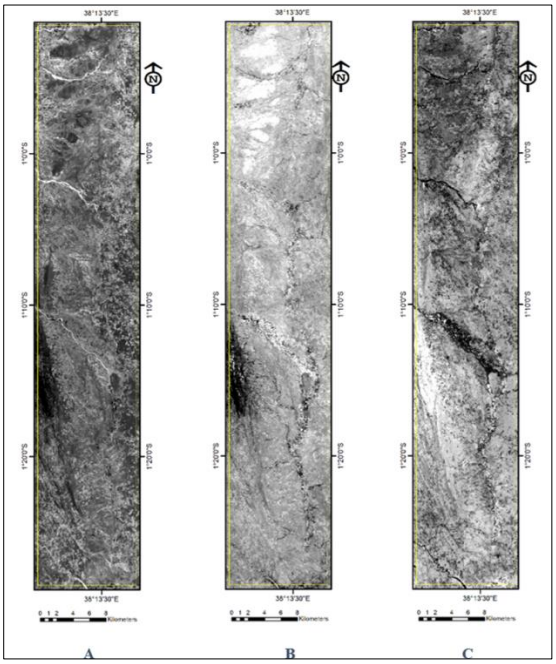

Figure 6: (A) Landsat 8 OLI/TIRS band ratio 4/2, enhances iron oxides in bright colour. (B) Landsat 8 band ratio 6/5, enhancing ferrous minerals in bright colour. (C) Landsat 8 band ratio 6/7 enhancing clays and hydroxyl minerals in bright colour.

The study area utilized Band Ratios 4/2, 6/7, and 6/5, commonly referred to as Sabins' Band Ratio, in the analysis. Sabins' Band Ratio (4/2, 6/7, and 6/5) has proven to be a valuable tool for lithological mapping and

detecting hydrothermal alteration zones. Band Ratio 4/2 is particularly effective for identifying iron-rich minerals often associated with hydrothermal alterations. Band Ratio 6/5 is useful for detecting iron oxides, while Band Ratio 6/7 is beneficial for delineating clay minerals such as illite, montmorillonite, and kaolinite [27].

Figure 6(A) presents the band ratio image 4/2 from Landsat 8 OLI/TIRS, which displays areas of reflection in band 4 and absorption in band 2. The image reveals zones of iron oxide alteration in bright white color, while regions of poor iron oxides are depicted in dark tones. Notably, there are a few areas of iron oxide enrichment in the Northeastern part of the region, while the rest of the area features minor patches scattered throughout. The diagram in Figure 6(B) showcases the band ratio 6/5 from the Landsat 8 OLI/TIRS image, depicting ferrous iron minerals in a bright white hue and areas devoid of such minerals in darker tones. The presence of ferrous minerals is evident in the northern region and extends into the central western section of the area.

The image depicted in Figure 6(C) is the band ratio 6/7 of Landsat 8 OLI/TIRS, which portrays clays and hydroxyl minerals in a bright white hue, and regions lacking these minerals appearing in a darker shade. The minerals are concentrated in the southwestern portion of the region, with a small, isolated area in the northeastern section.

Figure 7 presents the RGB color composite of the ratios 4/2-6/7-6/5, also known as Sabin's ratio[28]. This ratio was utilized to map lithologies and identify hydrothermal alteration zones. The presence of iron oxides in the image is indicated by a pink color, while clay and hydroxyl minerals are represented by a green hue. The dominant zones of ferrous minerals are illustrated in blue.

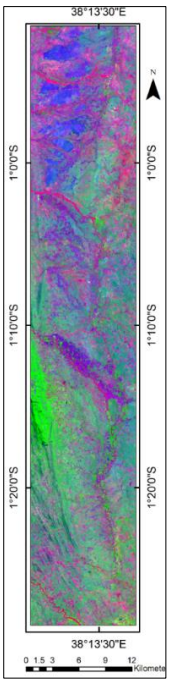

Figure 7: Sabin's composite band ratios (4/2-6/7-6/5 as RGB).

Principal component analysis

The principal component analysis was executed utilizing the seven spectral bands of the Landsat 8 Operational Land Imager (OLI) Thermal Infrared Sensor (TIRS), specifically bands 1, 2, 3, 4, 5, 6, and 7, as shown in the table below (see table 2).

Table 3: Principal component analysis of the study area (Eigenvector)

Input	Band 1	Band 2	Band 3	Band 4	Band 5	Band 6	Band 7	Eigen Values %
PC1	0.071	0.017	0.292	0.117	0.424	0.414	0.738	84.699
PC2	0.097	0.037	0.367	0.132	0.495	0.375	-0.672	11.972
PC3	0.175	0.109	0.457	-0.017	0.320	-0.801	0.068	1.650
PC4	0.311	0.081	0.642	0.000	-0.674	0.177	0.002	1.186
PC5	0.243	0.925	-0.216	-0.177	0.038	0.075	0.004	0.458
PC6	0.636	-0.096	-0.301	0.700	-0.024	-0.071	0.003	0.032
PC7	0.629	-0.338	-0.147	-0.668	0.130	0.073	-0.004	0.003

Table 3 displays the outcomes of the principal component analysis conducted using the seven optical bands (Band-1, Band-2, Band-3, Band-4, Band-5, Band-6, and Band-7). The results indicate that the first principal component (PC1) accounts for a significant proportion of the total variance in the data, amounting to 84.699%. Additionally, the second principal component (PC2) accounts for 11.972% of the total variance. Notably, the first three principal components (PC1, PC2, PC3) collectively account for a substantial portion of the total variance, amounting to 98.321%. The first principal component (PC1) exhibits the highest correlations with bands 7 (0.738), 6 (0.414), and 5 (0.424). This suggests that PC1 captures information about alteration minerals, such as iron oxides, clay minerals, and carbonates, which possess distinct absorption characteristics in the shortwave infrared (SWIR) region. PC2 displays high positive loadings on bands 5 (0.495), 6 (0.375), and 3 (0.367), as well as a high negative loading on band 7 (-0.672). This indicates that PC2 is associated with information related to vegetation and lithological differences. Finally, PC3 exhibits high positive loadings on bands 3 (0.457) and 5 (0.320), as well as a high negative loading on band 6 (-0.801). This suggests that PC3 captures information about ferrous iron minerals.

Image classification

In remote sensing, image classification involves attributing individual pixel elements or fundamental imagery units to distinct categorical labels. This procedure aims to aggregate homogeneous pixels derived from remotely acquired datasets into coherent classes aligned with users' interests through inter-pixel comparisons and comparison against reference samples of known identities. The efficacy of supervised classification hinges upon selecting appropriate training sites; a greater number of such sites typically yields improved outcomes [22].

To demonstrate this methodology, the study utilized a color composite of the Landsat 8 Operational Land Imager (OLI) using the Principal Component Analysis (PCA)-derived principal components PC3, PC2, and PC1 for the red, green, and blue channels, respectively, resulting in a thematic map illustrated in Figure 8. Supervised classification techniques were applied to this image, wherein predefined schemas or class categories were established. Regions characterized by clay/hydroxyl mineral distributions in the study area were primarily depicted in shades of purple on the generated maps, indicating higher concentrations of clays in the central and northern sections of Mui Basin (figure 9). By employing the geometry calculator tool in ArcGIS 10.8, the total surface area covered by clays in the basin was determined to be approximately 109 square kilometers.

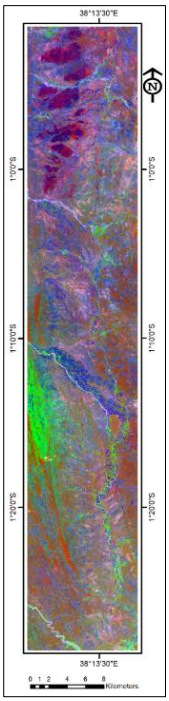

Figure 8: Colour Composite Of Landsat 8 OLI Image Using PC3, PC2 And PC1 In RGB. The Pink Color Represents Hydroxyls And Clay Minerals, The Green Pixels Represent Healthy Vegetation, The Blue Pixels Represent Bareland/Outcrops, And The Red Colour Represents Ferrous Minerals.

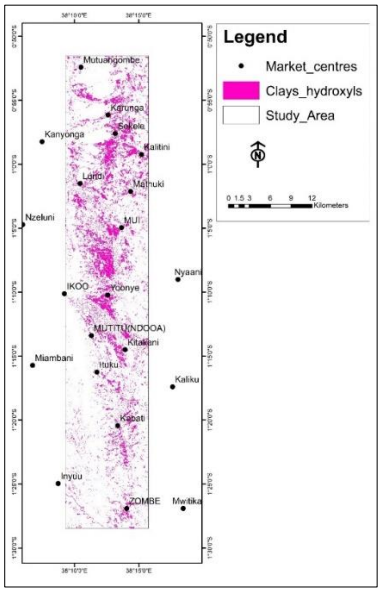

Figure 5: The Colour Composite Of Landsat 8 OLI Image Using PC3, PC2, And PC1 In RGB Was Used To Generate The Image Classification Above. The Purple Regions Represent The Clay/Hydroxyl Minerals Distribution In The Study Area.

Spectroscopy

During the survey, eight boreholes were used for the study conducted in the Mui basin. The specifics of these boreholes are outlined in Table 4 and their spatial distribution is displayed in figure 10.

Table 4: Illustrates the boreholes selected for the Mui Basin study.

Borehole	Easting	Northing	Elevation	Total Depth (mbgl)
COMM	412430	9875029	699	320.3
TOM10	411383	9871093	670	171.5
ZOM6	415215	9839396	692	138
MUT4	413679	9857865	681	264
KTZ4B	411979	9875778	692	241
YON7	412080	9871264	702	230.5
ZOM7	414973	9845397	690	159
ZOM8	413409	9840880	612	192

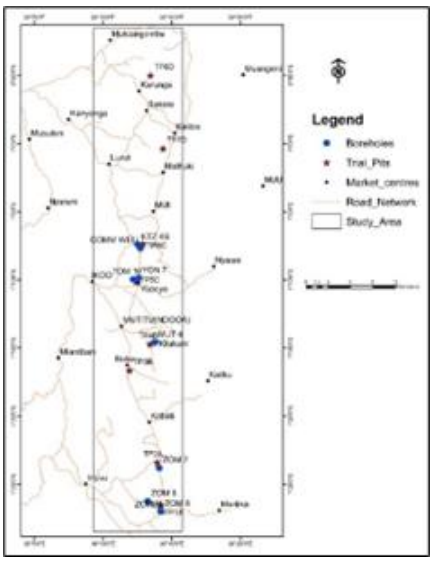

Figure 6: Presents visual representation of the general locations where boreholes and trial pits were sampled in the study area.

Spectroscopy examines the interactions between electromagnetic radiation (EMR) and matter, involving absorption, emission, or scattering of EMR [29]. In the short-wave infrared (SWIR) region, absorption characteristics are influenced by the mineral's composition [30]. These features result from energy absorption within the crystal lattice due to vibrational transitions between states. The distinct energy levels of these vibrational states lead to well-defined absorption features at specific wavelengths. The energy levels determining these wavelengths are dependent on the ionic radii sizes of the cations bonded to different molecules. Variation in bond lengths causes vibrations at different wavelengths. Consistent bond lengths between a particular atom and molecule enable the prediction of mineral compositions and changes by analyzing wavelengths and shifts in wavelength positions [29].

The absorption features at specific wavelengths result from transitions between energy levels and differences in composition. Table 5 illustrates the common clay minerals absorption feature positions.

Table 5: Major clay minerals related absorption feature positions *[31]*

Major Features positions	Molecule	Clay mineral
1.4µm	OH, and H_2O	Kaolinite/smectites/illites
1.9µm	H_2O	Smectites/illites
2.17µm	Al-OH	Kaolinite
2.2µm	Al-OH	Kaolinite/smectites/illites
2.29µm	Fe-OH	Smectites(nontronite)
2.3µm	Mg-OH	Smectites(hectorite)
2.34µm	Fe-OH/Mg-OH	Illite
2.384µm	Fe-OH	Kaolinite

Each mineral possesses a unique spectral fingerprint characterized by multiple absorption features influenced by factors such as composition, crystallinity, concentration, water content, and environmental factors.

Water molecules (H_2O) and hydroxyl (OH) produce diagnostic absorptions in clay minerals in the short-wave infrared (SWIR) wavelength region. The reflectance spectra of smectites, minerals containing water, exhibit characteristics reminiscent of water. Specifically, the initial overtone related to the stretching of OH appears at 1.4µm, while the one associated with the combination of H-O-H bending and OH stretching is observed around 1.9µm[1].

The spectrum of kaolinite is readily distinguished from the spectra of smectites because the kaolinite group clays do not have H_2O bands, except for halloysite (Bishop et al., 2008). Kaolinite spectra exhibit a sharp pair of bands due to the 2ύ(Al_2OH) stretching overtone at 1.396 and 1.416 um and a (ύ+σ) Al_2OH doublet at 2.17 and 2.21um [32]; [1]. Highly pronounced molecular water bands observed in desiccated samples suggest the presence of bound water characteristic of smectites, whereas prominent hydroxyl bands are typical of kaolinite [33]. In contrast, illite exhibits broader bands with lower absorption intensities for both features, attributed to the more randomly distributed hydroxyl within the octahedral sites [34].

The spectral analysis of all the soil samples collected from Mui Basin was conducted on 3rd April 2023 using Bruker Multi-Purpose Analyzer (MPA) at CIFOR-ICRAF's Soil-Plant Spectral Diagnostic Laboratory in Nairobi. The MPA is a Fourier-transform InfraRed (FTIR) Spectrometer that operates in the Near Infra-Red (NIR) wavebands region ([35]. The technique involved shining near-infrared light on the samples and capturing the diffused and reflected light into a raw file known as the interferogram within the electromagnetic spectrum range of 0.8µm to 2.5µm wavelength range. Through analysis, halloysite clay- a hydrated aluminum silicate- and montmorillonite and nontronite, belonging to the smectite clays family, were identified.

Hydrous aluminum silicates

Kaolinite, along with its less common variations like dickite and nacrite, belongs to a cluster of prevalent minerals known as hydrous aluminum silicates, constituting the primary components of kaolin, commonly referred to as china clay [36]. Additionally, this group encompasses halloysite and allophane. Typically observed as small, occasionally elongated hexagonal plates within compact or granular formations, and sometimes resembling mica-like accumulations, kaolinite, nacrite, and dickite emerge as natural byproducts of the alteration process affecting feldspars, feldspathoids, and various other silicates [37].

Halloysite

Halloysite, a clay found in various tropical and subtropical regions[38], exhibits a spectrum similar to kaolinite, but with the additional water bands near 1.9µm attributed to H_2O within its structure [32]. Figure 12 represents sample ID 505 and 506 from borehole TOM 10 at a depth between 139.9-141.4m and 166m-168m bgl and COMM Borehole at a depth between 111m -113m and 275m-277m bgl. The spectrum displays a sharp pair

of bands due to the 2ύ(Al_2OH) stretching overtone at 1.395µm and 1.415µm, and a (ύ+σ) Al_2OH doublet at 2.165µm and 2.209µm, and a water absorption band at 1.909µm. These spectral features are indicative of the presence of halloysite-type clays. Figure 11 illustrates halloysite clays spectra, and Table 6 shows sections where halloysite clays were encountered in Mui Basin. Halloysite clays were also discovered at the surface in Mikolosoni village and at 2.1m-3.2m bgl in a trial pit in the Kathozweni area of Mui Basin.

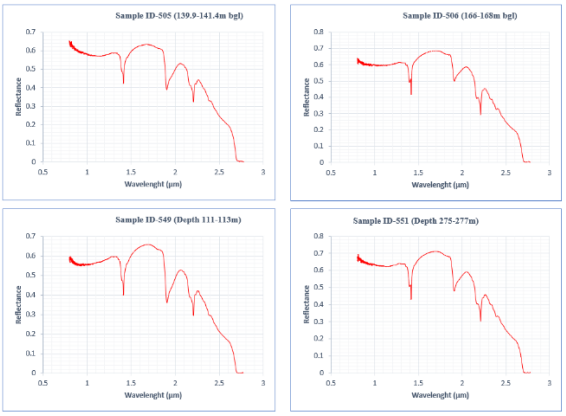

Figure 71: Characteristic halloysite absorptions in the SWIR spectra in sample ID 505, 506, and Sample ID 549, 551 from borehole TOM 10 and COMM, respectively. The doublet appearing at 1.395µm, 1.415 µm, 2.239µm and the water absorption band at 1.90µm is diagnostic for halloysite type of clays.

Table 6: Boreholes encountered Halloysite type of clays.

Well_name	Sample No	Top(m)	Bottom(m)	Clay type
COMM	549	111	113	Halloysite
COMM	551	275	277	Halloysite
TOM 10	504	87	90	Halloysite
TOM 10	505	139.9	141.4	Halloysite
TOM 10	506	166	168	Halloysite

Smectites

The term "Smectite" refers to a category of phyllosilicate minerals, with montmorillonite, beidellite, nontronite, saponite, and hectorite being the most significant species within this group[39].

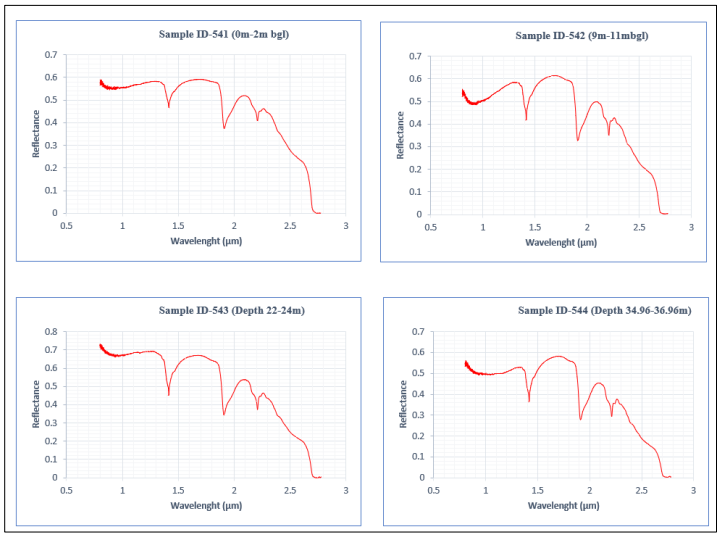

Figure 8: Spectral curve represents smectite clays in the COMM borehole. The spectra depict an H_2O stretching overtone at 1.41µm and an H_2O asymmetric combination band centered around 1.91µm.

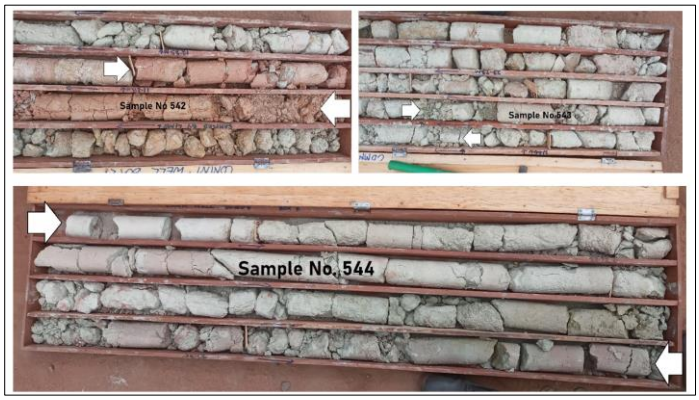

Figure 93: The depicted images illustrate the areas where samples 542, 543, and 544 were obtained from the COMM Borehole, and these sections consist solely of Smectite clays.

Smectites have identifiable bands for identification in the electromagnetic spectrum region of 1.0µm to 3.0µm (SWIR region). In the spectra of all smectites, there is an H_2O stretching overtone of (2v(H2O) observed at 1.41 µm, along with an H_2O asymmetric combination band of ((v+σ)as H2O) centered around 1.91µm[32]. The M-OH stretching and bending vibrations features depend on the presence of Al, $Fe^{3+,}$ or Mg cations in the octahedral sites and substitutions in the tetrahedral sites[32].

Sample 541, 542, 543, and 544 from COMM Borehole, collected at depths of 0-2m, 9-11m, 22m-24m and 34.96-36.96m below ground level (bgl) and depicted in Figure 12, exhibits a spectral band at 1.415µm attributed to water stretching overtone, a water combination band at 1.911µm, and a band at 2.209µm associated with Fe3+ or Mg cations in the octahedral sites. These characteristics strongly suggest the presence of montmorillonite-type clays[32]. According to Kariuki (2003), smectites typically display robust absorption bands near 1.40µm and 1.90µm, with an additional weaker band around 2.20µm, which is generally broad due to structural water. Kariuki also observed that in the absence of free water, the feature at 1.90µm becomes sharp and intense and shifts to lower wavelengths. The presence of smectite clays was identified in the boreholes outlined in Table 7 and depicted in Figure 13, which were evaluated in the Mui basin.

Table 7: Boreholes that intercepted Smectite clays in Mui Basin

Borehole name	Top(m)	Bottom(m)	Clay type
COMM	0	82	Smectite
KTZ 4B	3	176	
MUT 4	199	263	
TOM 10	1	23	
YON 7	6.83	212	
ZOM 6	6	137	
ZOM 7	15	156.5	
ZOM 7	136	137	

Nontronite

The nontronite, a type of smectite clay, was detected in well ZOM 8, well MUT 4, and surface sample 751. In well MUT 4, nontronite was encountered between 6.0m and 41.0m below ground level, while in ZOM 8, it was encountered between 2.0m and 161.0m below ground level (see Table 8, fig 14 & 15). Nontronite clays exhibited the common spectral characteristics of smectite clays; it has spectral band 2v (Fe^{3+} 2OH) at 1.415 µm and (ύ+σ) Fe^{3+} 2OH band at 2.29 µm (see figure 15). An additional shoulder at 2.24 µm observed in Nontronite samples is associated with stretching plus bending combination band (ύ+σ) $AlFe^{3+}$ OH [32]. Nontronite is the iron-rich end member of the smectite group of clay minerals. It has a high iron content, typically around 30% Fe2O3 [40]. It forms as an alteration product of iron-rich igneous and metamorphic rocks, hydrothermal deposits, and some marine sediments.

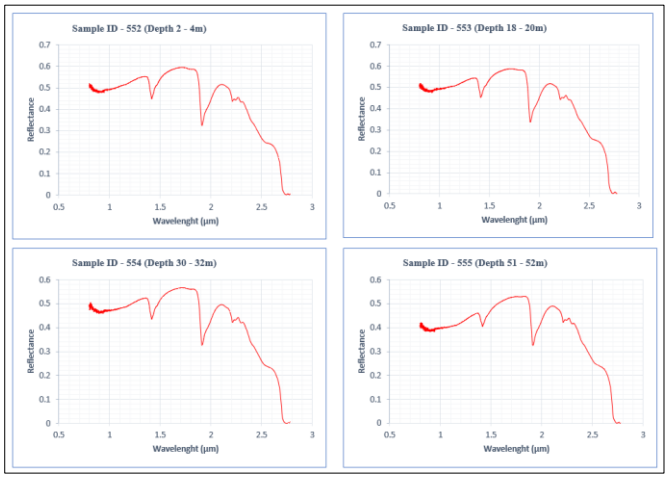

Figure 14: Spectra of samples 552, 553, 554, and 555 taken from Borehole ZOM 8 between the depths of 2m-4m, 18m-20m, 30m-32m, and 51m-52m bgl. The spectra indicate the presence of nontronite clays in the borehole.

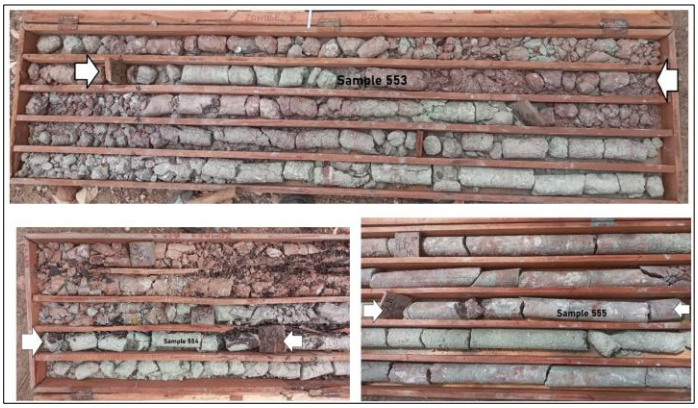

Figure 10: The depicted images illustrate the areas where samples 553, 554, and 555 were obtained from the COMM borehole, and these sections consist solely of nontronite clays.

Table 8: The boreholes and the depth at which nontronite clays were encountered.

Borehole name	Sample No	Top(m)	Bottom(m)	Clay type
MUT 4	538	6	8	Nontronite
MUT 4	539	19	21	
MUT 4	562	153	155	
ZOM 8	552	2	4	
ZOM 8	553	18	20	
ZOM 8	554	30	32	
ZOM 8	555	51	52	
ZOM 8	556	81	83	
ZOM 8	557	123	125	
ZOM 8	558	159	161	

IV. Discussions

Spectral analysis is considered one of the most sophisticated remote sensing methods for characterizing clay minerals [41]. This study applied a combination of spectral analysis and remote sensing to study the Mui Basin clay minerals.

The application of a remote sensing enhancement method has proved beneficial in delineating clay minerals within the region. Analysis of color composites, particularly the false-color composite comprising bands 5, 6, and 7 in RGB, facilitated the differentiation of bare land, hydrothermally altered rocks, and vegetation cover. The hydrothermally altered rocks exhibited a blue hue, consistent with Lincoln et al.'s 2019 research conducted in the southern vicinity adjacent to the study area.

The band ratio enhancement method was employed to identify features not visible in raw bands[42]. Sabin's band ratios (4/2, 6/7, and 6/5) effectively detected hydrothermal alteration zones, with the 6/7 ratio beneficial for delineating clays and hydroxyl minerals (illite, montmorillonite and kaolinite) appearing in bright colours.

Lincoln et al. (2019) noted that vegetation density consistently limits detection when mapping hydrothermally altered rocks using band composites. Hence, principal component analysis (PCA) was utilized to mitigate these effects in lithological mapping. The colour composite of Landsat 8 OLI image employing PC3, PC2, and PC1 in RGB effectively delineated clay/hydroxyl minerals, appearing in pink hues. The PCA image was also used to conduct image classification, facilitating the extraction of clay minerals and developing a clay distribution map of the Mui basin.

Spectral analyses were utilized to determine the type and mineralogy of clay fractions within the Mui basin. Two distinct types were identified: smectite and halloysite. Smectite clays were found in Boreholes COMM, KTZ 4B, ZOM 7, TOM 10, YON 7, ZOM 6, and sections of MUT 4. The spectral signature of smectites included vibration bands at 1.415µm related to water stretching overtone, a water combination band at 1.911µm, and a band at 2.209µm associated with Fe^{3+} or Mg cations in the octahedral sites. These characteristics strongly indicate the presence of montmorillonite-type clays[32].

Smectites, mainly montmorillonite dominate the clay composition within the Mui Basin. While Montmorillonite is often linked to the hydrothermal alteration of volcanic ashes [41], its prevalence extends to soils with limited drainage, allowing for solution concentration through evaporation [43]. This scenario is characteristic of hydromorphic, calcimorphic soils found in warmer climates. In regions with inadequate drainage, where evaporation leads to accumulation of silica, alumina, magnesia, and often iron within an alkaline environment rich in Mg^{2+} and Ca^{2+} ions, similar to conditions observed in the Mui Basin.

Nontronite, an iron (III) rich member of the smectite group of clay minerals, was identified in Boreholes ZOM 8 and MUT 4. It shares typical spectral features of smectites clays, including a spectral band at 1.415 µm (2v (Fe3+ 2OH)) and a (ύ+σ) Fe3+ 2OH band at 2.29 µm. Additionally, a shoulder at 2.24 µm, observed in Nontronite samples, indicates the presence of a stretching plus bending combination band (ύ+σ) AlFe3+ OH, suggesting the presence of Al^{3+} in the clays. The provenance of nontronite is similar to the smectite group of clay minerals.

Halloysite was detected in Borehole TOM 10 between depths of 166m to 168m below ground level (bgl), and in Borehole COMM between 111m to 277m bgl. The spectrum displays a sharp pair of bands due to the 2ύ(Al2OH) stretching overtone at 1.395µm and 1.415µm, and a (ύ+σ) Al2OH doublet at 2.165µm and 2.209µm, and a water absorption band at 1.909µm. Halloysite occurs widely in both weathered rocks and soils, and it has been identified as having formed by alteration of a wide variety of types of both igneous and non-igneous rocks[44].

Smectite clays find diverse applications across various industries. In the oil and geothermal drilling sector, they are a crucial component of drilling mud, enhancing viscosity for efficient drilling operations (Zhang et al., 2020). Additionally, smectites are utilized in foundry sand and desiccants to absorb moisture from air and gases[6]. In agriculture, it is added to drought-prone soils as a soil additive to retain moisture. Moreover, smectites play a pivotal role in construction projects, such as earthen dams and levees, to prevent fluid leakage [9].

The swelling property of smectites makes it an ideal material for various applications, including protective liners for landfills and annular seals for water wells [45]; [46]; [47]. Additionally, Na-montmorillonite is utilized in cat litter products due to its adsorbent and clumping properties [48].

Beyond industrial applications, smectites and Halloysite are used in cosmetics [49] and as a coagulant in pond water treatment, attracting and settling minute particles [50]. While effective in absorbing heavy metals (Gkouma et al., 2021), its impact on human health remains uncertain[51]. Montmorillonite has been explored for external use in treating contact dermatitis (Park et al., 2016) and added to animal foods as an anti-caking agent. Furthermore, it has been extensively employed in catalytic processes and in papermaking to minimize deposit formation and improve drainage [52].

V. Conclusions

Spectroscopy and remote sensing have proven to be effective in characterizing the different types of clays found in the Mui basin. The results indicate that the Mui basin primarily comprises smectite-type clays, with only a few localities of Halloysite and nontronite clays. The provenance of these clays can be attributed to the hydromorphic and calcimorphic environment of the basin, where inadequate drainage and high evaporation led to the accumulation of silica, alumina, magnesia, and iron in an alkaline environment rich in Mg^{2+} and Ca^{2+} ions. These findings provide valuable insights into the geological history and formation of the Mui Basin clays, which can inform future research and development in various industries, including construction, oil drilling, and environmental remediation. Further studies can explore these clays' potential applications and unique properties, contributing to the development of more sustainable and efficient materials and technologies.

Acknowledgments

The research work was made possible through the generous support of the African Development Bank (AfDB) via a scholarship provided by the Institute of Geothermal Training and Research at the Dedan Kimathi University of Technology. The Ministry of Energy and Petroleum, specifically the Coal exploration department, granted access to all the Boreholes drilled in the Mui Basin, facilitating valuable data collection. Vicopat Geological and Geotechnical Consultants Limited funded the fieldwork and laboratory assays, ensuring the successful completion of this research endeavor.

References

[1] P. C. Kariuki, "Spectroscopy And Swelling Soils An Integrated Approach," Phd Thesis, Delft University Of Technology, Netherlands, 2003.
[2] O. Canbaz, Ö. Gürsoy, And A. Gökce, "Detecting Clay Minerals In Hydrothermal Alteration Areas With Integration Of Aster Image And Spectral Data In Kösedag-Zara (Sivas), Turkey," J. Geol. Soc. India, Vol. 91, No. 4, Pp. 483–488, Apr. 2018, Doi: 10.1007/S12594-018-0882-1.
[3] O. O. Osinowo, A. Gomy, And M. Isseini, "Mapping Hydrothermal Alteration Mineral Deposits From Landsat 8 Satellite Data In Pala, Mayo Kebbi Region, Southwestern Chad," Sci. Afr., Vol. 11, P. E00687, Mar. 2021, Doi: 10.1016/J.Sciaf.2020.E00687.
[4] A. F. H. Goetz And L. C. Rowan, "Geologic Remote Sensing," Sci. Ser., Vol. 211, Pp. 781–791, 1981.
[5] J. K. Mitchell And K. Soga, Fundamentals Of Soil Behavior, Third Edition. John Wiley & Sons, Inc, 1993.
[6] N. Yaghmaeiyan, M. Mirzaei, And R. Delghavi, "Montmorillonite Clay: Introduction And Evaluation Of Its Applications In Different Organic Syntheses As Catalyst: A Review," Results Chem., Vol. 4, P. 100549, Jan. 2022, Doi: 10.1016/J.Rechem.2022.100549.
[7] L. Lichner, P. Hallett, D. Feeney, O. Ďugová, M. Šír, And M. Tesar, "Field Measurement Of Soil Water Repellency And Its Impact On Water Flow Under Different Vegetation," Biologia (Bratisl.), Vol. 62, Pp. 537–541, Oct. 2007, Doi: 10.2478/S11756-007-0106-4.
[8] K. K. Kennedy, K. J. Maseka, And M. Mbulo, "Selected Adsorbents For Removal Of Contaminants From Wastewater: Towards Engineering Clay Minerals," Open J. Appl. Sci., Vol. 8, No. 8, Art. No. 8, Aug. 2018, Doi: 10.4236/Ojapps.2018.88027.
[9] M. Kociánová, R. Drochytka, And V. Černý, "Technology Of Remediation Of Embankment Dams By Optimal Grout," Procedia Eng., Vol. 151, Pp. 257–264, Dec. 2016, Doi: 10.1016/J.Proeng.2016.07.370.
[10] H. Mohamed El-Desoky, N. Soliman, M. Ahmed Heikal, And A. Moustafa Abdel-Rahman, "Mapping Hydrothermal Alteration Zones Using Aster Images In The Arabian–Nubian Shield: A Case Study Of The Northwestern Allaqi District, South Eastern Desert, Egypt," J. Asian Earth Sci. X, Vol. 5, P. 100060, Jun. 2021, Doi: 10.1016/J.Jaesx.2021.100060.
[11] J. Zhang, M. Xu, G. E. Christidis, And C. Zhou, "Clay Minerals In Drilling Fluids: Functions And Challenges," Clay Miner., Vol. 55, Pp. 1–24, Apr. 2020, Doi: 10.1180/Clm.2020.10.
[12] E. M. Mathu, "The Mutito And Ikoo Faults In The Pan-African Mozambique Belt, Eastern Kenya," Basement Tecton. 7, Pp. 61–69, 1992, Doi: 10.1007/978-94-017-0833-3_5.
[13] L. D. Sanders, "Geology Of The Kitui Area," Geological Survey Of Kenya, Nairobi, 30, 1954.
[14] A. Crowther, "Geology Of The Mwingi Area, North Kitui: Degree Sheet 45, Nw Quarter: With Coloured Geological Map," No Title.
[15] L. Sanders, "Geology Of Kitui Area, Report 30," Geol. Surv. Kenya, 1954.
[16] R. G. Rejith And S. Mayappan, "Mapping Of Mineral Resources And Lithological Units: A Review Of Remote Sensing Techniques," Int. J. Image Data Fusion, Vol. 10, Pp. 1–28, Apr. 2019, Doi: 10.1080/19479832.2019.1589585.
[17] M. Imbroane, C. Melenti, And D. Gorgan, Mineral Explorations By Landsat Image Ratios. 2007, P. 340. Doi: 10.1109/Synasc.2007.52.
[18] B. M. Omwenga, "Geothermal Well Site Suitability Selection Using Geographic Information Systems (Gis) And Remote Sensing: Case Study Of The Eburru Geothermal Field".
[19] J. R. Beattie And F. W. L. Esmonde-White, "Exploration Of Principal Component Analysis: Deriving Principal Component Analysis Visually Using Spectra," Appl. Spectrosc., Vol. 75, No. 4, Pp. 361–375, Apr. 2021, Doi: 10.1177/0003702820987847.
[20] A. Bishta, "Lithologic Discrimination Using Selective Image Processing Technique Of Landsat 7 Data, Um Bogma Environs Westcentral Sinai, Egypt," J. King Abdulaziz Univ.-Earth Sci., Vol. 20, Jan. 2009, Doi: 10.4197/Ear.20-1.10.
[21] C. Kujjo, "Application Of Remote Sensing For Gold Exploration In The Nuba Mountains, Sudan." Accessed: Aug. 17, 2024. [Online]. Available: Https://Www.Semanticscholar.Org/Paper/Application-Of-Remote-Sensing-For-Gold-Exploration-Kujjo/F8cebf62c4fbbf295ba090d4db5ef13b359ab0d3
[22] C. Palaniswami, A. K. Upadhyay, And M. H.P, "Spectral Mixture Analysis For Subpixel Classification Of Coconut," Curr. Sci., Vol. 91, Dec. 2006.
[23] F. Calderón, M. Haddix, R. Conant, K. Magrini-Bair, And E. Paul, "Diffuse-Reflectance Fourier-Transform Mid-Infrared Spectroscopy As A Method Of Characterizing Changes In Soil Organic Matter," Soil Sci. Soc. Am. J., Vol. 77, P. 1591, Sep. 2013, Doi: 10.2136/Sssaj2013.04.0131.
[24] M. Li, G. Luo, Y. Li, Y. Qin, J. Huang, And J. Liao, "Effects Of Landscape Patterns And Their Changes On Ecosystem Health Under Different Topographic Gradients: A Case Study Of The Miaoling Mountains In Southern China," Ecol. Indic., Vol. 154, P. 110796, Oct. 2023, Doi: 10.1016/J.Ecolind.2023.110796.
[25] M. Ge, S. Fang, Y. Gong, P. Tao, G. Yang, And W. Gong, "Understanding The Correlation Between Landscape Pattern And Vertical Urban Volume By Time-Series Remote Sensing Data: A Case Study Of Melbourne," Isprs Int. J. Geo-Inf., Vol. 10, P. 14, Jan. 2021, Doi: 10.3390/Ijgi10010014.
[26] L. K. Githenya, P. C. Kariuki, And A. K. Waswa, "Application Of Remote Sensing In Mapping Hydrothermal Alteration Zones And Geological Structures As Areas Of Economic Mineralization In Mwitika-Makongo Area, Se Kenya," 2019.
[27] K. Banerjee, M. Jain, S. Panda, And A. Jeyaseelan, "Landsat 8 Oli Data For Identification Of Hydrothermal Alteration Zone In Singhbhum Shear Zone Using Successive Band Depth Difference Technique–A New Image Processing Approach," Curr. Sci., Vol. 116, Pp. 1639–1647, May 2019, Doi: 10.18520/Cs/V116/I10/1639-1647.
[28] F. F. Sabins, "Remote Sensing For Mineral Exploration," Ore Geol. Rev., Vol. 14, No. 3–4, Pp. 157–183, 1999.
[29] P. Hauff, "An Overview Of Vis-Nir-Swir Field Spectroscopy As Applied To Precious Metals Exploration," Spectr. Int. Inc, Vol. 80001, Jan. 2008.
[30] G. R. Hunt, "Spectral Signatures Of Particulate Minerals In The Visible And Near Infrared," Geophysics, Feb. 2012, Doi: 10.1190/1.1440721.

[31] P. Hauff, "An Overview Of Vis-Nir-Swir Field Spectroscopy As Applied To Precious Metals Exploration," Spectr. Int. Inc, Vol. 80001, Pp. 303–403, 2008.
[32] J. L. Bishop, J. R. Michalski, And J. Carter, "Remote Detection Of Clay Minerals," In Developments In Clay Science, Vol. 8, Elsevier, 2017, Pp. 482–514. Doi: 10.1016/B978-0-08-100355-8.00014-X.
[33] G. R. Hunt, "Visible And Near-Infrared Spectra Of Minerals And Rocks: I Silicate Minerals," Mod. Geol., Vol. 1, Pp. 283–300, 1970.
[34] H. Mathews, R. Cunningham, And G. Petersen, "Spectral Reflectance Of Selected Pennsylvania Soils," Soil Sci. Soc. Am. J., Vol. 37, No. 3, Pp. 421–424, 1973.
[35] Dickens Ateku, "Standard Operating Procedures For Sample Analysis Using Bruker Multi-Purpose Analyzer (Mpa) Fourier Transformation Near Infrared Spectrometer," World Agroforestry Centre, Nairobi, Standard Operating Procedures Sop 006, Sep. 2021. [Online]. Available: Http://Worldagroforestry.Org/Research/Land-Health
[36] Bitannica, "Kaolinite | Clay Mineral, Aluminium Silicate, Hydrated Aluminium | Britannica." Accessed: Aug. 17, 2024. [Online]. Available: Https://Www.Britannica.Com/Science/Kaolinite
[37] J. Forsyth, Characterisation Of Minerals Using Evolved Gas Analysis And Infrared Spectroscopy. Sheffield Hallam University (United Kingdom), 2001.
[38] Y. Xia, M. Rubino, And R. Auras, "Interaction Of Nanoclay-Reinforced Packaging Nanocomposites With Food Simulants And Compost Environments," In Advances In Food And Nutrition Research, Vol. 88, Academic Press, 2019, Pp. 275–298. Doi: 10.1016/Bs.Afnr.2019.02.001.
[39] I. E. Odom, "Smectite Clay Minerals: Properties And Uses," Philos. Trans. R. Soc. Lond. Ser. Math. Phys. Sci., Vol. 311, No. 1517, Pp. 391–409, Jun. 1984, Doi: 10.1098/Rsta.1984.0036.
[40] L. Cipriano Crapina, L. Dzene, J. Brendlé, F. Fourcade, A. Amrane, And L. Limousy, "Clay-Modified Electrodes In Heterogeneous Electro-Fenton Process For Degradation Of Organic Compounds: The Potential Of Structural Fe (Iii) As Catalytic Sites," Materials, Vol. 14, No. 24, P. 7742, 2021.
[41] Ü. Altinbaş, Y. Kurucu, M. Bolca, And A. El-Nahry, "Using Advanced Spectral Analyses Techniques As Possible Means Of Identifying Clay Minerals," Turk. J. Agric. For., Vol. 29, No. 1, Pp. 19–28, 2005.
[42] A. S. Ali And A. B. Pour, "Lithological Mapping And Hydrothermal Alteration Using Landsat 8 Data: A Case Study In Ariab Mining District, Red Sea Hills, Sudan," Int. J. Basic Appl. Sci., Vol. 3, No. 3, P. 199, 2014.
[43] M. Bradshaw, "Origin Of Montmorillonite Bands In The Middle Jurassic Of Eastern England," Earth Planet. Sci. Lett., Vol. 26, No. 2, Pp. 245–252, 1975.
[44] E. Joussein, S. Petit, J. Churchman, B. Theng, D. Righi, And B. Delvaux, "Halloysite Clay Minerals—A Review," Clay Miner., Vol. 40, No. 4, Pp. 383–426, 2005.
[45] M. Asada And S. Horiuchi, "High-Density Bentonite Slurry For Seepage Barriers," J. Mater. Civ. Eng., Vol. 17, No. 2, Pp. 178–187, 2005.
[46] A. Corina Et Al., "Application Of Bentonite As An Alternative Sealing Material For Deep Hydrocarbon And Geothermal Wells," Presented At The Arma Us Rock Mechanics/Geomechanics Symposium, Arma, 2021, P. Arma-2021.
[47] D. A. Reid-Soukup And A. L. Ulery, "Smectites," Soil Mineral. Environ. Appl., Vol. 7, Pp. 467–499, 2002.
[48] J. P. Ferris, "Montmorillonite-Catalysed Formation Of Rna Oligomers: The Possible Role Of Catalysis In The Origins Of Life," Philos. Trans. R. Soc. B Biol. Sci., Vol. 361, No. 1474, Pp. 1777–1786, 2006.
[49] K. Chen, B. Guo, And J. Luo, "Quaternized Carboxymethyl Chitosan/Organic Montmorillonite Nanocomposite As A Novel Cosmetic Ingredient Against Skin Aging," Carbohydr. Polym., Vol. 173, Pp. 100–106, 2017.
[50] M. Sultana, M. Wulandari, And Y. Adachi, "Remarkable Potential Of Na-Montmorillonite As A Sustainable And Eco-Friendly Material For Flocculant Studied In The Standardized Mixing Flow," Bioresour. Technol. Rep., Vol. 23, P. 101567, 2023.
[51] B. Lothenbach, G. Furrer, And R. Schulin, "Immobilization Of Heavy Metals By Polynuclear Aluminium And Montmorillonite Compounds," Environ. Sci. Technol., Vol. 31, No. 5, Pp. 1452–1462, 1997.
[52] A. Vanerek, B. Alince, And T. Van De Ven, "Delamination And Flocculation Efficiency Of Sodium-Activated Kaolin And Montmorillonite," Colloids Surf. Physicochem. Eng. Asp., Vol. 273, No. 1–3, Pp. 193–201, 2006.